ACS Sustainable Chemistry & Engineering

pubs.acs.org/journal/ascecg

Research Article

Regulation of Electron Transfer and Microstructure in RuN Single-Atom Catalysts and Their Catalytic Performance for CO/CO_2 Hydrogenation

Haojie Geng,*,⊥ Haobo Zhao,⊥ Le Yang, Zhuwan Li, Jingyu Ran,* and Nian Bing Li*

Cite This: https://doi.org/10.1021/acssuschemeng.5c01497

Read Online

ACCESS | Metrics & More | Article Recommendations | Supporting Information

ABSTRACT: In this study, we developed a new type of Ru−N−C single-atom catalyst (SAC) with an excellent catalytic performance for CO/CO_2 selective hydrogenation. RuN SACs were synthesized by constructing defects in the support with different coordination numbers and anchoring Ru species onto these vacancies. Three RuN_x SACs (x = 2, 3, and 4) were synthesized: RuN_2 and RuN_4 SACs, which were obtained by direct calcination, and RuN_3, which was obtained by high-temperature shock (HTS). HTS combined electrostatic adsorption and strong thermal coupling to anchor Ru atoms to N vacancies with a novel three-dimensional structure. The resulting RuN SACs exhibited excellent catalytic performance for the selective methanation of CO/CO_2; in particular, RuN_3 achieved a CO conversion of 99% and a CH_4 selectivity of 95% under a gas hourly space velocity (GHSV)of 4255 h^{-1} at 150 °C. Electron transfer was observed between the Ru and N species, facilitating the formation of electron-deficient centers over the catalyst surface, which actively captured CO molecules, even at low CO pressures. Moreover, RuN SACs facilitated the breakage of the C−O chemical bond during the CO hydrogenation reaction and formation of a highly selective alkane product (CH_4). Although the hydrogenation of CO_2 was performed simultaneously, its reactivity was lower, and only a small amount of CO gas was released to the atmosphere. Additionally, Ru atoms in RuN_3 possessed a unique protruding structure supported by the N species, which interacted with the reaction species at a high flux. Therefore, our novel RuN SACs can completely remove the CO species from H_2-rich gas, which is beneficial for the stable operation of proton-exchange membrane fuel cells (PEMFCs).

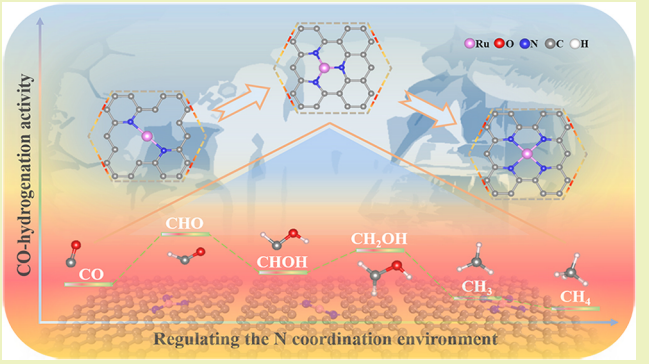

KEYWORDS: *CO hydrogenation, CO_2 hydrogenation, RuN SACs, electron transfer, microstructures*

1. INTRODUCTION

In proton-exchange membrane fuel cells (PEMFCs), a low CO concentration in H_2-rich gas has a strong toxic effect on the Pt electrode.[1−3] As such, the CO concentration should be reduced to less than 10 ppm, particularly at low temperatures, to ensure the optimal operation of PEMFC. CO hydroconversion is an effective method of deep CO removal. In practical applications, CO_2 is commonly present in H_2-rich gases, and its hydrogenation process is often accompanied by a reverse water−gas shift (RWGS) reaction, leading to secondary CO formation. For example, the Ni-0.15In/CeO_2 catalyst developed by Xiao et al.[4] achieves a CO selectivity of 99.6% at 400 °C, but with a CO_2 conversion rate as high as 38.5%, where RWGS-generated CO weakens the removal efficiency. Similarly, Zhang et al.[5] reported that Ni−$In_{0.5}$/SBA-15 exhibits 99% CO selectivity at 400 °C, yet with a CO_2 conversion rate of 29%. These findings indicate that conventional catalysts struggle to achieve both efficient CO methanation and CO_2 suppression, highlighting the importance of developing catalysts with high CO selectivity and CO_2 inertness.

In nanoparticle (NP) catalysts composed of Ni[6−10]Ru[11−15]Rh[16−20]etc., the hydrogenation of carbon oxides can produce methane and higher hydrocarbons with low selectivity during CO/CO_2 hydrogenation.[21−25] In this context, single-atom catalysts (SACs)[26−30]owing to their unique geometric and electronic properties, offer new strategies for precisely tuning hydrogenation pathways. In SAC synthesis based on metal−organic frameworks (MOFs),[31,32]high-temperature pyrolysis facilitates the formation of stable metal-N coordination bonds,[33−37]effectively preventing metal atom aggregation. Studies have shown that the nitrogen coordination environment plays a crucial role in regulating the competitive

Received: February 18, 2025
Revised: May 14, 2025
Accepted: May 15, 2025

adsorption of CO and CO_2. For instance, Qiao et al.[38] found that Au SACs preferentially adsorb CO via 5d orbital vacancies, while Lou et al.[39] demonstrated that different nitrogen coordination numbers (GN_x, x = 1/4, 2, 3, and 4) differentially modulate the activity of CO_2 reduction to CO, providing key insights for selectively inhibiting CO_2 reactions.

For CO hydrogenation mechanisms,[40,41] Zhao et al.[42] eval-evaluated the intermediates during CO methanation to determine the optimal metal pairs that can effectively break C−O bonds and simultaneously hydrogenate *C/*O with low energy barriers, which is crucial for achieving high methanation under mild conditions. CO tends to be independently adsorbed at the top sites. For Ru-based catalysts, C atoms adopt sp hybridization to form a short σ(Ru−C) bond (1.88 Å), resulting in their high adsorption capacity. Zhang et al.[43] obtained the activation barrier of 1.29 eV for the hydrogenation of the C end of CO to form a CHO intermediate with a reaction energy of 0.93 eV, which was significantly lower than that through a COH intermediate. This suggests that *CHO is the mainstream reaction pathway for CO hydrogenation, whereas *CO is the mainstream reaction pathway for the hydrogenation of CO_2 on Ru-based catalysts.

Although several studies have investigated the factors affecting the catalytic activity of oxide-supported Ru systems, the catalytic activity of a single Ru atom for the CO/CO_2 hydrogenation is rarely reported. For instance, Song et al.[44] constructed a CeZrO/Ni inverse interface under low-temperature (200 °C) and high space velocity (15,000 mL·g^{-1}·h^{-1}) conditions, enabling the efficient conversion of CO via dual formate and *CO pathways while preventing intermediate self-poisoning at low temperatures, achieving a CO conversion rate of 90% (close to the thermodynamic equilibrium value). Additionally, Zhou et al.[45] demonstrated that under 200 °C light irradiation, the Ru/CeO_2−H catalyst exhibited a methane production rate of 275.1 mmol·g^{-1}·h^{-1}, 1.5 times higher than that of pure thermal catalysis. In situ diffuse reflectance infrared Fourier transform spectroscopy (DRIFTS) analysis confirmed that the formate pathway was dominant, while the *CO pathway also contributed. To address this research gap, we simulated an N-coordinated Ru SAC using density functional theory (DFT) to predict its catalytic activity for CO/CO_2 hydrogenation. We then synthesized Ru SACs with different N coordination numbers using a MOF. Finally, we performed catalytic performance tests, characterizations, and DFT calculations to explore the relationship between the structure and performance of the catalysts. The resulting RuN SACs satisfied the demand for CO removal in small H_2-production machines.

2. EXPERIMENTAL SECTION

2.1. Synthesis of RuN SACs. RuN SACs were synthesized via a ZIF-8-derived protocol combining controlled pyrolysis and rapid thermal shock to modulate the Ru−N coordination environment. First, a Zn^{2+}/Ru^{3+}-doped ZIF-8 precursor was obtained by coprecipitating Zn^{2+} and Ru^{3+} with 2-methylimidazole, which confines Ru within the MOF cages. Pyrolysis at 1100 °C under N_2 removed Zn and collapsed the framework, yielding an N-doped carbon matrix with atomically dispersed RuN_2 sites (RuN_2(C)). Subsequent NH_3 treatment at 900 °C enriched surface nitrogen, converting RuN_2(C) into a four-coordinate RuN_4(C) phase. For RuN_3(C), a ZnN_4@SAC intermediate was formed by low-temperature pyrolysis (400 °C), followed by Zn removal, Ru^{3+} adsorption, and a 1200 °C/100 ms Ar thermal shock to lock Ru into a trigonal N_3 coordination. For comparison, Ru nanoparticles were synthesized by a conventional wet impregnation on SiO_2. This hierarchical approach—tuning atmosphere, temperature profile, and kinetics—enables precise control over Ru−N coordination numbers (2−4) for rational SAC design. Detailed experimental procedures are provided in Supporting Information S1.1.

2.2. Catalytic Performance Measurements. The catalytic performance of Ru SACs and Ru NPs was evaluated in a fixed-bed flow reactor under conditions simulating the crude gas from methanol reforming. Catalyst loadings (0.1−10.0 g) were chosen according to the surface active-site density determined by chemisorption, and were diluted 1:10^4 (w/w) with quartz sand to ensure differential (<10%) conversion. The mixture was packed into a quartz tube (i.d. ≈ 6 mm), secured by quartz wool, and a thermocouple was inserted at the bed center for real-time temperature control and monitoring of endo/exothermic signals. After in situ reduction with 5 vol % H_2/N_2 at 2 °C/min, the feed was switched to a quaternary gas (70% H_2, 20% CO_2, 1% CO, balance N_2) at 100 mL/min (GHSV ≈ 4255 h^{-1}). Effluent gases were sampled (50 μL) and analyzed online by GC (Beifen Ruili SP-3420A) with a flame-ionization detector. CO and CO_2 conversions were calculated as

$$X_{CO} = \frac{F_{CO,in} - F_{CO,out}}{F_{CO,in}} \times 100\% \quad (1)$$

$$X_{CO_2} = \frac{F_{CO_2,in} - F_{CO_2,out}}{F_{CO_2,in}} \times 100\% \quad (2)$$

where $F_{CO,in}$, $F_{CO,out}$ are the molar flow rates of CO at the reactor inlet and outlet, respectively, $F_{CO_2,in}$ and $F_{CO_2,out}$ are the molar flow rates of CO_2 at the reactor inlet and outlet, respectively. For further experimental details, see Supporting Information Section S1.2.

2.3. Materials Characterization. Powder X-ray diffraction (XRD) patterns were collected on a Beijing Puxi XD-6 diffractometer using Cu Kα radiation (λ = 0.15406 nm) at 36 kV and 20 mA over 2θ = 10−80° with a scan rate of 4°/min; crystallite sizes were estimated via the Scherrer equation (K = 0.89). Textural properties were evaluated by N_2 physisorption on a Micromeritics ASAP 2020 HD88 Plus after degassing (350 °C, 4 h), with surface areas calculated by Brunauer−Emmett−Teller (BET) and pore distributions calculated by BJH. Ru loadings were determined by inductively coupled plasma optical emission spectroscopy (ICP-OES) (PerkinElmer Optima 3000 DV). Morphology and dispersion were examined by transmission electron microscopy (TEM) (FEI Talos F200X, 200 kV), high-angle annular dark-field-scanning TEM/energy dispersive X-ray spectroscopy (HAADF-STEM/EDS) (Hitachi HD3000C, 200 kV, aberration-corrected), and STEM-EDX mapping; samples were drop-cast from ethanol suspensions. High resolution TEM (HRTEM) image simulations were carried out in Dr. Probe (100−300 kV, Cs = 1 mm, Cc = 1.5 mm) and benchmarked against DFT-relaxed structures. Surface chemical states were probed by X-ray photoelectron spectroscopy (XPS) (SPECS MCD-10, Al Kα, 1486.6 eV), with Ru 3d/N 2p spectra deconvoluted in Peak-Fit 6.0 and referenced to adventitious C 1s (284.8 eV). In situ Ru K-edge XAS was performed at NSRF beamlines 8-ID and 8-BM (10 keV, 2 scans min^{-1}) under reaction conditions, using a Ru foil for energy calibration and IFEFFIT/EaVX for data processing. In situ Fourier transform infrared spectroscopy (FTIR) spectra were recorded in transmission mode (PerkinElmer, MCT detector, 0.1 cm^{-1} resolution) on catalyst wafers (~1 cm Θ) under heating and CO pulse adsorption; full deconvolution details are provided in the Supporting Information. The detailed information on these measurements is described in Supporting Information S1.3.

2.4. DFT Calculation Details. DFT calculations were conducted using the Vienna Ab initio Simulation Package (VASP) with the projector-augmented wave (PAW) method and the Perdew−Burke−Ernzerhof (PBE) functional under the generalized gradient approximation (GGA). A plane-wave energy cutoff of 400 eV was applied, and spin polarization along with dipole corrections were included. The Ru SACs were modeled on a single-layer (3 × 3) graphene substrate with a vacuum region of ~15 Å to avoid interlayer

https://doi.org/10.1021/acssuschemeng.5c01497
ACS Sustainable Chem. Eng. XXXX, XXX, XXX−XXX

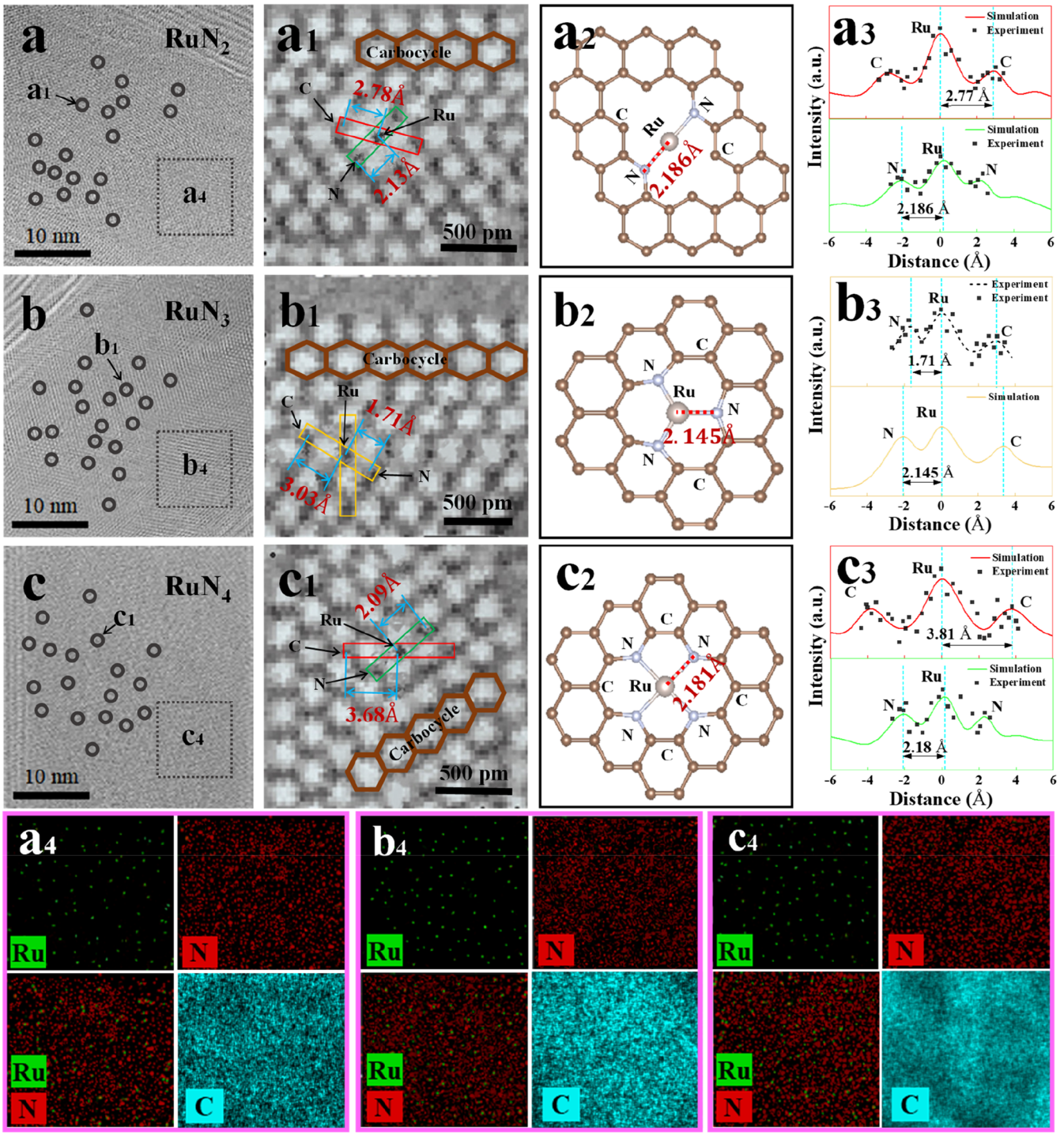

Figure 1. Morphology of Ru SACs characterized by 2D HRTEM and EDS method. (a–c) HRTEM images of Ru SAC; (a1–c1) representative Ru active site (single atom) and the distances of Ru–N and Ru–C species; (a2–c2) DFT calculation models for Ru SACs; (a3–c3) comparison of intensity vs distance in a selected region between experimental and simulation results; (a4–c4) distribution of Ru, N, and C species characterized by the EDS method.

interactions. A Monkhorst–Pack *k*-point grid of 4 × 4 × 1 was used for energy and geometry optimization, and 6 × 6 × 1 was used for electronic structure analysis. The calculations incorporated zero-point energy and entropy contributions to obtain Gibbs free energies, and adsorption energies were determined based on the total energy differences between the adsorbed and isolated systems. The d-band centers were calculated from the projected density of states. Detailed computational parameters and models are provided in Supporting Information S1.4.

3. RESULTS AND DISCUSSION

This study investigated the properties of Ru SACs, including their morphology, active sites, coordination, chemical bonds, etc. Their catalytic performance, electron transfer, and reaction intermediates were characterized by using a fixed-bed reactor through in situ techniques, DFT calculations, and other characterization tests. The Ru SACs exhibited excellent catalytic performance for CO removal in a H_2-rich atmosphere.

https://doi.org/10.1021/acssuschemeng.5c01497
ACS Sustainable Chem. Eng. XXXX, XXX, XXX–XXX

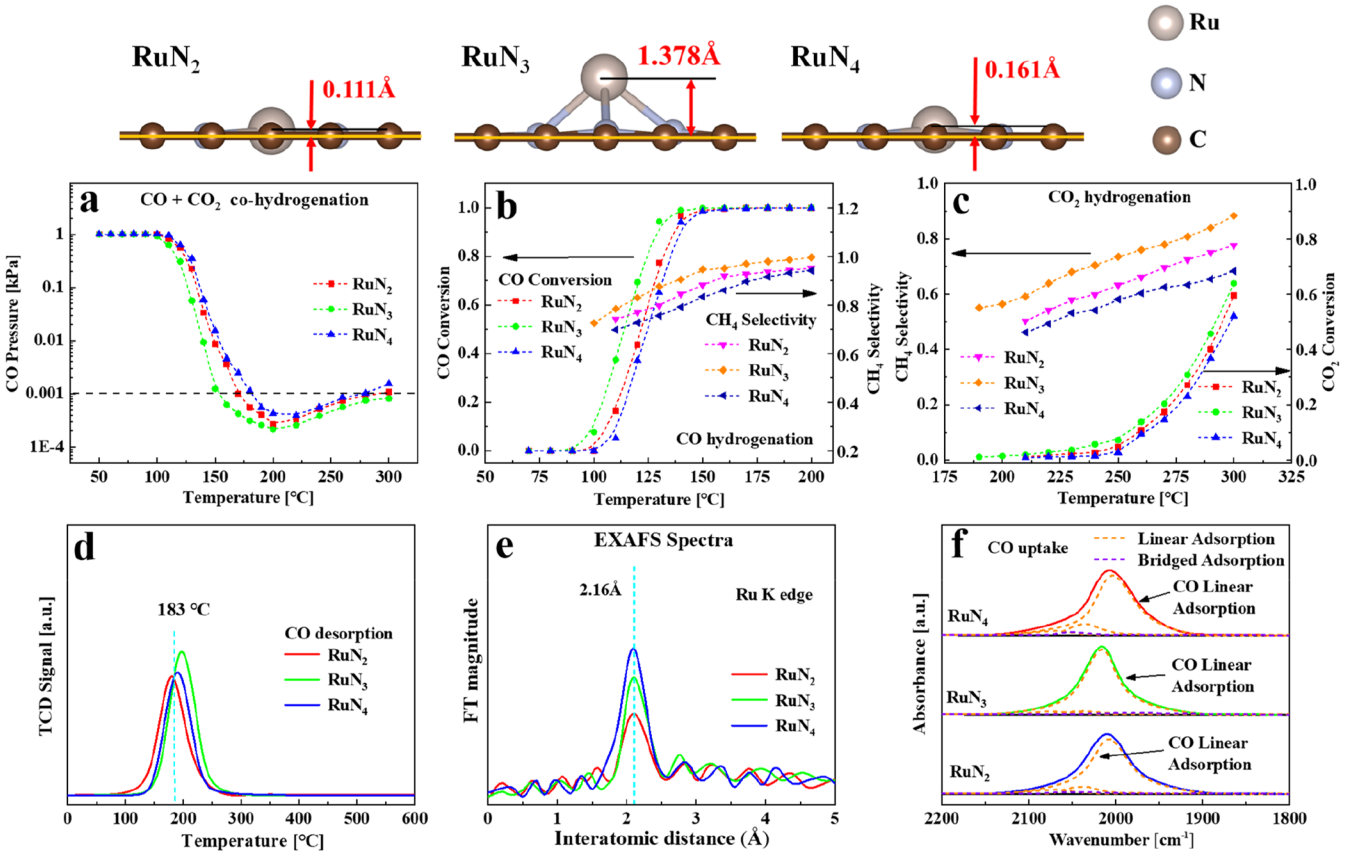

Figure 2. Catalytic performance of CO/CO_2 cohydrogenation via the three Ru SACs (a), CO conversion and product selectivity (b), CO_2 conversion and product selectivity (c), desorption curves of Ru SACs chemisorbed by CO (CO-TPD) (d); R space of EXAFS spectra (Ru K-edge) for Ru SACs (e), and infrared spectra measured during CO uptake over Ru SACs (f).

3.1. Morphology of Ru SACs. The Ru SACs coordinated with N species were synthesized by using different types of vacancies generated by sublimation, adsorption, and high-temperature shock (HTS) techniques. The specific surface areas and crystal lattices of the SACs were characterized using Brunauer−Emmett−Teller (BET) measurements and X-ray powder diffraction (XRD), as shown in Figures S7 and S8. Simulated high-resolution transmission electron microscopy (HRTEM) images of the Ru SACs were obtained using commercial software Dr. Probe (Figure S9). The HRTEM simulation results were consistent with the DFT calculation results.

Figure 1a−c shows an overview of the Ru SACs. Figure 1a1−c1 presents representative Ru active sites for the distance measurement of Ru−N and Ru−C bonds and their comparison with the DFT simulation data. The two-dimensional (2D) HRTEM images of the representative Ru active sites are similar to the simulated images in Figure S9. The distances of the Ru−N bonds are 2.13 Å (RuN_2) and 2.09 Å (RuN_4), which correspond with the DFT calculation results of 2.186 Å (RuN_2) and 2.181 Å (RuN_4), respectively. However, the Ru−N distance of the RuN_3 sample is only 1.71 Å, which is lower than that of the DFT calculation result (2.145 Å). Figure 1a3−c3 presents a comparison of the variations in intensity with the distance. Figure S10 shows the detailed DFT simulation results of the Ru SACs, in which the Ru active sites can be observed at horizontal and vertical viewing angles. The Ru atoms in the RuN_2 and RuN_4 samples remain in the same plane as the surrounding N and C atoms, with the offset distances of 0.111 and 0.161 Å for RuN_2 and RuN_4, respectively. In the RuN_3 sample, the Ru atoms are not retained in the same plane as the surrounding atoms. In particular, the distance between the Ru atom and the N−C plane is 1.378 Å, explaining the difference in the distance obtained by the HRTEM and DFT simulations. Such a unique three-dimensional configuration is beneficial for surface-active sites to capture CO species and, as a result, promote deep CO removal during hydrogenation reactions.

Figure 1a4−c4 displays the Ru, N, and C distribution in the Ru SAC samples characterized by energy-dispersive X-ray spectroscopy (EDS). The Ru species were atomically dispersed on the surface and coordinated with the surrounding N atoms. The three Ru SAC samples have similar Ru mass loadings of 0.5−0.6 wt %. Meanwhile, the N mass loading increases from 17.16 to 23.63 wt %, enhancing the N vacancies and coordination number. The C species have the highest proportion among the three elements. The Ru, N, and C proportions were measured by using inductively coupled plasma optical emission spectrometry (ICP-OES) (Table S3). The C evaporation is lower during high-temperature treatments.

Figure 2 shows the catalytic performances and relative properties of the three Ru SACs, as characterized using a fixed-bed reactor, temperature-programmed reaction (TPR), extended X-ray absorption fine structure (EXAFS), and infrared (IR) spectroscopy. The reaction feed gas comprised a 1 kPa CO, 20 kPa CO_2, 70 kPa H_2, and N_2 balance. The feed gas was injected into the catalyst bed for CO/CO_2 cohydrogenation

https://doi.org/10.1021/acssuschemeng.5c01497
ACS Sustainable Chem. Eng. XXXX, XXX, XXX−XXX

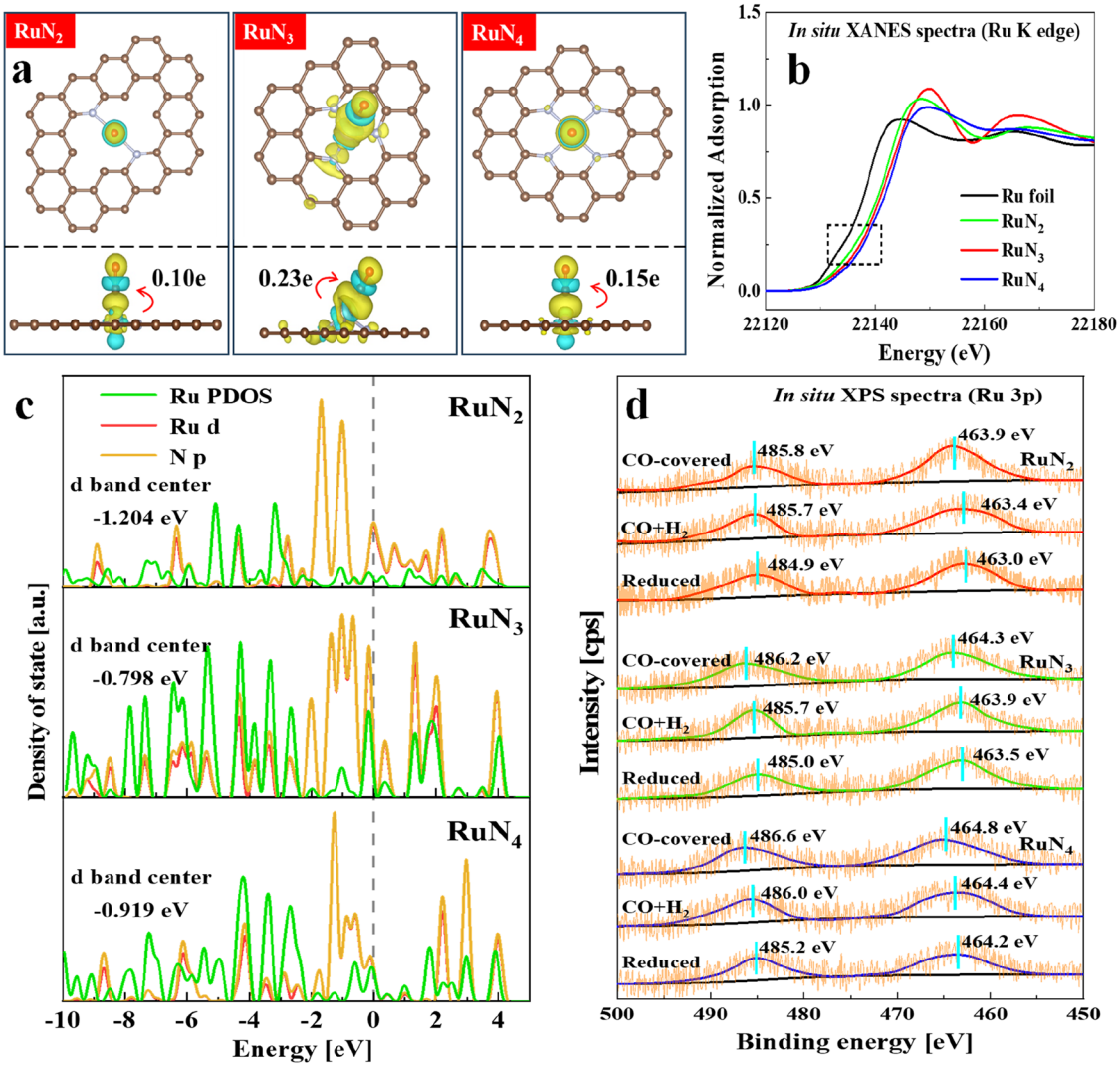

Figure 3. Structures and electron transfer of Ru SACs under CO chemisorption (a), the *in situ* XANES spectra (Ru K-edge) measured under CO hydrogenation for RuN SACs (b), density of state and d-band center calculated from DFT simulations (c), and the *in situ* XPS spectra (Ru 3p) of Ru SACs under different reaction conditions (d).

over the Ru SACs. The catalytic performance is shown in Figure 2a. The CO pressure decreased rapidly, reaching 0.001 kPa at 150−180 °C. At approximately 200 °C, the CO pressure decreases to the lowest value and then increases again, owing to CO_2 hydrogenation, which forms a large amount of CO and increases the CO concentration.

Figures 2b and S13 show the conversion, pressure, selectivity, and C distribution during CO hydrogenation with the feed gas composed of 1 kPa of CO, 70 kPa of H_2, and N_2 balance. In contrast to the results reported in the literature, where a CO conversion rate of only 60% is achieved at 200 °C, in this study, the CO conversion rapidly approaches 100% within the temperature range of 100−150 °C, significantly surpassing the typical requirement of over 250 °C to achieve a conversion rate of more than 80% as reported in the literature.[46−48] As the feed gas did not contain CO_2, the hydrogenation of CO_2 to CO did not occur. As a result, the CO pressure did not increase at higher temperatures. CH_4 is the main product of the RuN SACs, followed by methanol. Ru NPs exhibit a lower CO conversion rate at 150−200 °C and notably lower CH_4 selectivity in comparison to those of the RuN SACs.

Figures 2c, S14, and S15 show the conversion, selectivity, and C distribution during CO_2 hydrogenation over the Ru catalysts, respectively. CO_2 hydrogenation over Ru SACs requires temperatures of more than 250 °C. The reaction product is mainly composed of CH_4, similar to that for CO hydrogenation, followed by CH_3OH. The catalytic activity of the Ru NPs for CO_2 hydrogenation is considerably lower than that of the Ru SACs. Furthermore, excess CO was formed over the Ru NPs, whereas low CO selectivity was noted for the Ru SACs. Such low-concentration CO gases could be continuously hydrogenated and eliminated. Among the three RuN SACs, RuN_3 exhibited the best hydrogenation performance because the Ru atoms, which are active sites, are not in the same plane as the N and C atoms. In particular, the distance of the Ru atoms to the C/N plane is 1.378 Å for RuN_3, which is considerably higher than that of RuN_2 (0.111 Å) and RuN_4 (0.161 Å), thereby contributing to variations in the binding energy, coordination, exposure probability, etc.

Figure 2d shows the desorption curves of the CO gas chemisorbed onto Ru SACs, as obtained by temperature-programmed desorption (TPD). The CO species first flows and is adsorbed over the Ru SACs, and then the physically

https://doi.org/10.1021/acssuschemeng.5c01497
ACS Sustainable Chem. Eng. XXXX, XXX, XXX−XXX

adsorbed CO is detached under vacuum. CO-TPD was performed in a He atmosphere at increasing temperatures. The chemisorbed CO species are desorbed from the Ru SACs. The three Ru SACs display similar CO-TPD curves with the desorption temperature of approximately 180 °C.

The EXAFS spectra (Ru K-edge) of the fresh RuN SACs were obtained, as shown in Figures 2e and S16, to demonstrate the atomically dispersed Ru atoms. The three RuN SACs exhibit similar R distances of 2.16 Å. The coordination numbers are displayed in Table S4. The coordination numbers of the Ru−N pair are 2.05, 3.30, and 4.50 for RuN_2, RuN_3, and RuN_4, respectively. The coordination numbers are in good agreement with the DFT simulation and HRTEM results. Figure S17 shows the good stability of the RuN SACs, whereby the catalytic performance and EXAFS results remained nearly unchanged after 800 h of hydrogenation. This stability not only confirms its reliability in industrial applications but also highlights its strong resistance to deactivation, which contributes to reducing catalyst replacement frequency, thereby minimizing resource consumption and operational costs.

Figure 2f shows the IR spectrum measured from the Ru SACs chemisorbed by the CO species. CO chemisorption can be classified as linear, bridged, or multiple adsorption (Table S6). For the Ru SACs, linear CO adsorption is the main adsorption mechanism because highly dispersed sites can be adsorbed only point-to-point. Ru crystal facets can be obtained from Ru NPs, and the infrared spectra in Figure S18 show the adsorption of various CO species. However, such adsorption of various forms is unsuitable for evaluating surface-active sites using CO probes. As bridged and multiple adsorptions exist on the catalyst surface, the quantitative relationship between the CO and surface sites is unclear. Thus, the CO probe can be used only to evaluate the number of Ru surface sites of the Ru SACs. The results of CO chemisorption are presented in Figure S19 and Table S7. We compared the results obtained with those of the ICP-OES method, where good agreement was depicted.

Based on the number of active sites, we normalized the reaction rate over each active site and obtained the variations in activation energies under catalytic conditions (Figure S20). From the perspective of the catalytic mechanism, the RuN_3 site exhibits the lowest activation energy (73 kJ/mol), which is closely related to its unique electronic structure. The three-coordination structure not only maintains an appropriate electron density at the metal center but also provides an optimal geometric configuration for substrate adsorption, thereby effectively reducing the energy barrier for transition state formation. In contrast, the relatively higher activation energy of the RuN_4 site (84 kJ/mol) may be attributed to its rigid coordination structure, which diminishes the substrate proximity. Meanwhile, the intermediate activation energy of the RuN_2 site (77 kJ/mol) reflects the electron-enriching effect at the metal center due to a reduction in the coordination number. Overall, these differences in kinetic parameters validate, from an energetic perspective, the role of the nitrogen coordination environment in electronically modulating the catalytic active centers, thereby providing key thermodynamic insights for the rational design of efficient Ru-based catalysts.

The electronic structures of the surface-active sites determine the adsorption and reaction behaviors of the reactants. Owing to the interaction between Ru and the coordinated N atoms, charge transfer and electric cloud distribution can be controlled by varying the N coordination number. Figure 3a shows the structures and electron transfer of the Ru SACs under CO chemisorption, as obtained by a DFT simulation. From the Ru active sites to the CO molecules, 0.10e, 0.23e, and 0.15e electrons transfer for the RuN_2, RuN_3, and RuN_4 samples, respectively. CO chemisorption causes variations in the surface electronic structures of the Ru SACs, as compared in Figure S21 and Table S8. In particular, some electrons transfer to the CO molecules, whereas others are transferred to the N atoms, resulting in greater losses of Ru electrons. The RuN_3 SAC, with the highest electron loss, has the highest binding energy toward adsorbed molecules (Figure S22), such as CO and CO_2. A strong combination is conducive to the selective capture of CO molecules and their deep removal.

Figure 3b shows the in situ X-ray absorption near-edge structure (XANES) spectra (Ru K-edge) measured during CO hydrogenation with the feed gas composed of 1 kPa of CO, 10 kPa of H_2, and Ar balance. The three RuN SACs exhibit similar chemical states under CO hydrogenation. The reduced electron transfer in the Ru foil resulted in its lower K-edge energy than that of the RuN SACs. Figure S23 displays the XANES Spectra (Ru K-edge) of the Ru SACs measured under H_2-reduced, CO hydrogenation, and fully covered conditions. The RuN_3 sample has the largest energy variation with and without CO chemisorption.

In the RuN_x (x = 2−4) coordination system, the d-band center of Ru atoms exhibits a nonmonotonic trend, initially shifting upward and then downward as the nitrogen coordination number increases. This behavior is directly related to changes in the occupancy of the CO $2\pi^*$ antibonding orbitals. Previous research has shown that if the energy level of the electron is close to the Fermi level, they are more active and prone to interacting with reactant molecules, primarily because of their higher energy and lower energy barriers. These electrons can easily migrate from the solid to the reactant molecules, thereby promoting catalytic performance. The density of states (DOS) distributions of the three Ru single-atom catalysts, as shown in Figure 3c, indicate that the d-band centers are −1.204, − 0.798, and − 0.919 eV for RuN_2, RuN_3, and RuN_4, respectively. Among them, RuN_3 has the d-band center closest to the Fermi level, suggesting higher catalytic activity. This is corroborated by activity tests, which demonstrate that RuN_3 achieves the highest CO conversion at a lower reaction temperature. These findings confirm that RuN_3, with its unique conical coordination structure, optimizes the d-band center position and surface charge distribution, selectively promoting hydrogenation of CO to CH_4 rather than deep carbon-chain growth. This coordination configuration represents the optimal balance among activity, selectivity, and stability.

Figure 3d shows the *in situ* X-ray photoelectron spectroscopy (XPS) spectra (Ru 3p) of the Ru SACs measured under different reaction conditions. The samples were reduced in H_2 and kept under vacuum for the XPS measurements. "CO + H_2" indicates CO hydrogenation with 0.01 mbar of CO and 0.1 mbar of H_2 at 150 °C. The CO-covered samples were kept in a 0.02 mbar of CO atmosphere to achieve full chemisorption. With increasing CO coverage, the binding energies of Ru $3p^{1/2}$ and Ru $3p^{3/2}$ both increase, indicating that the $\sigma-\pi$ interaction of CO induces electron transfer from Ru to CO, leading to partial oxidation of Ru ($Ru^{\delta+}\rightarrow CO^{\delta-}$). The increase in binding energy shows a dependence on the coordination environment:

https://doi.org/10.1021/acssuschemeng.5c01497
ACS Sustainable Chem. Eng. XXXX, XXX, XXX−XXX

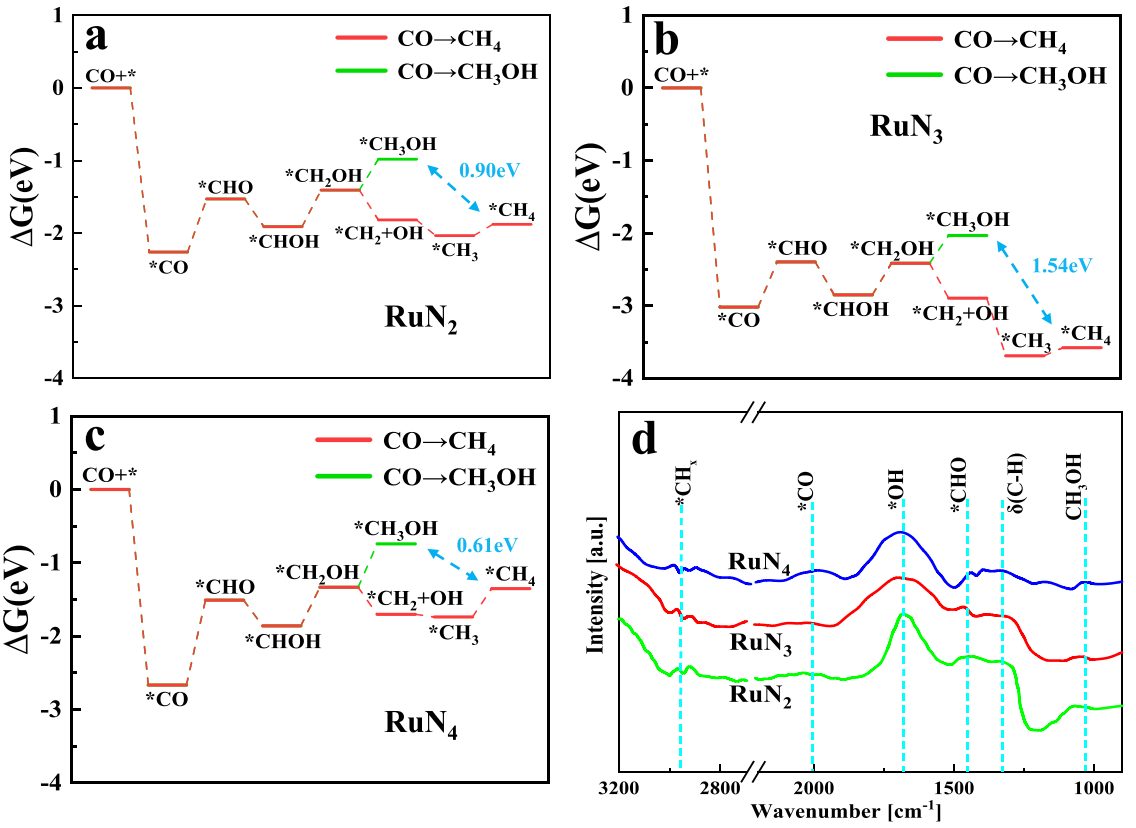

Figure 4. DFT simulation of the hydrogenation of CO to methane or to methanol over Ru SACs: RuN_2 (a), RuN_3 (b), and RuN_4 (c). The "*in situ*" DRIFTS spectra measured under reaction conditions (d).

RuN_2 (484.9 eV) < RuN_3 (485.0 eV) < RuN_4 (485.2 eV), suggesting that as the number of coordinated nitrogen atoms increases, the electron feedback capability of Ru decreases, thus exacerbating the oxidation state shift induced by CO adsorption. This electronic state change affects the CO activation process: the high electron density of Ru weakens the C≡O bond by π-back-donation, providing a thermodynamic driving force for CO activation. Furthermore, as shown in the in situ XPS spectrum of Ru 3p (Figure S24), Ru species can be divided into three chemical valences: Ru^0, Ru^{3+}, and Ru^{4+}. Ru in RuN SACs is mainly composed of ionic Ru species ($Ru^{\delta+}$), whereas metallic Ru species (Ru^0) comprise a large portion of Ru NPs. In addition, the N 1s XPS spectrum (Figure S25) reveals that five types of nitrogen species are present in the RuN SACs: oxidized graphitic N, graphitic N, pyrrolic N, Ru−N, and pyridinic N. The Ru−N states comprised a large proportion of the total N species.

We performed DFT simulations to display all of the reaction pathways and elucidate the reaction mechanisms of the RuN SACs during CO hydrogenation, as shown in Figure 4a−c. Two hydrogenation pathways were identified: the methane and methanol pathways. CO chemisorption onto the Ru active sites (*CO) was the initial reaction step for CO hydrogenation. Several intermediates, such as *CO, *CH_1OH, *OH, and *CH_x, may accumulate on the surface, owing to their low reactivity. Among these, *CH_2OH is an important intermediate species that produces CH_4 upon its breakdown into *CH_2 and *OH. The energies of the CH_4 pathway are lower than those of the methanol pathway with differences of 0.90, 1.54, and 0.61 eV for RuN_2, RuN_3, and RuN_4, respectively. The values and optimized stable configurations are shown in Figures S26−31. Figures S32 and S33 present the CO hydrogenation over Ru NPs for comparison.

Various free radicals, such as *OH, *CH_x, *CHO, and *CO, are detected in in situ diffuse reflectance infrared Fourier transform spectroscopy (DRIFTS) spectra. The spectral variations as the temperature was increased from 120 to 200 °C are shown in Figure S34. The CO absorption peak gradually decreases as the temperature increases. High temperatures increase the reactivity of CO hydrogenation and consumption of *CO species, decreasing the intensity of the CO peak. Figure 4d presents the results at a representative temperature of 200 °C to compare the three RuN SACs. In the 2850−3000 cm^{-1} region, a weak yet reproducible C−H stretching vibration peak was detected, indicating the formation of alkyl species within the system. The low signal intensity may be attributed to the rapid conversion of *CH_3 into CH_4, preventing the accumulation of alkyl intermediates. This observation aligns with the computational results of the free energy profile, which suggest a low energy barrier for the *CH_3→CH_4 transition. Additionally, a broadened absorption band observed at 1678 cm^{-1} corresponds to the OH stretching vibration of surface hydroxyl radicals (*OH), suggesting the dissociation of oxygen atoms from hydrocarbon groups. Notably, the RuN_3 catalyst exhibits a stronger absorption signal in this region, which may indicate its enhanced ability to stabilize oxygen-containing intermediates, thereby influencing the catalytic reaction pathway.

The reaction pathway analysis during CO_2 hydrogenation is important because it involves the formation of a CO product that should be restricted. The main products of the CO_2 hydrogenation are CH_4, methanol, and CO. Figures S35−S43

https://doi.org/10.1021/acssuschemeng.5c01497
ACS Sustainable Chem. Eng. XXXX, XXX, XXX−XXX

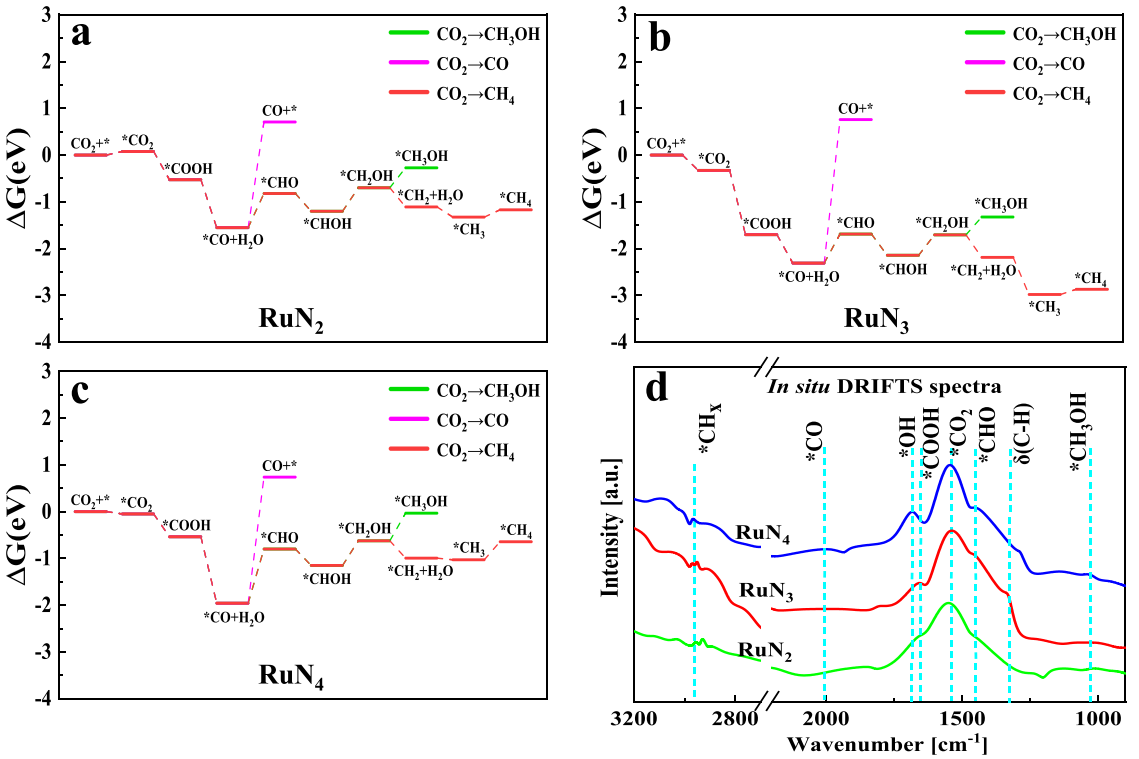

Figure 5. DFT simulation of the hydrogenation of CO_2 to different carbon products over Ru SACs: RuN_2 (a), RuN_3 (b), and RuN_4 (c). The "*in situ*" DRIFTS spectra measured under CO_2 hydrogenation (d).

displays the variation in the Gibbs free energy of the three RuN SACs and their optimized intermediate configurations under CO_2 hydrogenation. The CO_2 hydrogenation over each RuN SACs followed three reaction pathways, namely that of CO, CH_4, and methanol. The reaction pathways are compared in Figure 5a−5c. Methanation has the lowest energy, making it the optimal pathway. CO is an intermediate generated during hydrogenation. However, the desorption of the CO species is difficult, and a large amount of CO is further converted to *CHO to form other hydrocarbon products. As a result, few CO species are released into the atmosphere, ensuring deep CO removal.

Similar to the CO hydrogenation, the in situ DRIFTS spectra exhibit various free radicals including *OH, *CH_x, *CO_2, *CO, *CHO, and *COOH. Figure 5d presents the results at a representative temperature of 280 °C for comparison. The IR spectra obtained at different temperatures are shown in Figure S44. A characteristic peak at 1710 cm^{-1}, corresponding to the C═O stretching vibration in *COOH, indicates that CO_2 preferentially adsorbs on the catalyst surface and is rapidly protonated to form COOH. Meanwhile, the signal at 2050 cm^{-1}, attributed to the C≡O stretching vibration in *CO, appears only briefly at lower temperatures before disappearing, suggesting that CO is generated only during the initial stage of the reaction and is subsequently hydrogenated to *CHO. As the temperature increases, the intensities of the peaks at 2920 cm^{-1} (assigned to the C−H stretching vibration in *CH_2) and 2850 cm^{-1} (assigned to the symmetric stretching of *CH_3) gradually increase, concurrent with the decay of the *COOH signal, indicating that C−O bond cleavage remains the rate-determining step. Notably, the RuN_3 sample exhibits the strongest *CH_x signals during this process, further confirming its enhanced CH_4 selectivity in the CO_2 hydrogenation.

4. CONCLUSIONS

In this study, we developed novel RuN SACs and investigated their catalytic performances in terms of conversion, selectivity, and stability during CO/CO_2 hydrogenation. The conclusions are as follows:

1. Three types of Ru−N coordination pairs were observed over the RuN SACs, namely RuN_2, RuN_3, and RuN_4. The RuN_3 sample exhibited a unique three-dimensional structure with its Ru active site offset from the N−C crystal plane, resulting in its superior catalytic performance.
2. The RuN SACs, especially the RuN_3 sample, exhibited good performance in deep CO removal. Moreover, the side reaction of CO_2 hydrogenation did not contribute to the release of CO to the atmosphere.
3. The electron transfer between the Ru and N species facilitated the formation of electron-deficient centers on the catalyst surface, facilitating the breakage of the C−O chemical bond and producing hydrocarbon species (CH_4).
4. After continuous operation at 170 °C for 800 h, the RuN SAC system (particularly the RuN_3 sample) maintained excellent catalytic activity, with less than a 3% decline. This result provides a sustainable chemical solution characterized by high atom economy (metal utilization >99%) and low-carbon processing, holding promise for advancing green catalytic manufacturing from laboratory scale to industrial scale.

■ ASSOCIATED CONTENT

Supporting Information

The Supporting Information is available free of charge at https://pubs.acs.org/doi/10.1021/acssuschemeng.5c01497.

https://doi.org/10.1021/acssuschemeng.5c01497
ACS Sustainable Chem. Eng. XXXX, XXX, XXX−XXX

Detailed experimental procedures and operational protocols; material synthesis methods and reagent sources; XRD diffraction patterns and phase identification; BET specific surface area and pore size distribution analysis; catalytic performance testing and activity evaluation data; XPS surface chemical state analysis; in situ XAS structural characterization; FT-IR vibrational mode assignments and adsorbate identification; CO chemisorption and active site quantification; DFT model descriptions, energy barrier analyses, and electronic structure representations (PDF)

AUTHOR INFORMATION

Corresponding Authors

Haojie Geng − *School of Chemistry and Chemical Engineering, Chongqing Key Laboratory of Soft-Matter Material Chemistry and Function Manufacturing, Southwest University, Chongqing 400715, China;* orcid.org/0000-0003-0208-0190; Email: hjgeng@swu.edu.cn

Jingyu Ran − *School of Energy and Power Engineering, Key Laboratory of Low-grade Energy Utilization Technologies and Systems, Ministry of Education, Chongqing University, Chongqing 400044, China;* orcid.org/0009-0009-1467-6160; Email: ranjy@cqu.edu.cn

Nian Bing Li − *School of Chemistry and Chemical Engineering, Chongqing Key Laboratory of Soft-Matter Material Chemistry and Function Manufacturing, Southwest University, Chongqing 400715, China;* orcid.org/0000-0001-6395-2074; Email: linb@swu.edu.cn

Authors

Haobo Zhao − *School of Chemistry and Chemical Engineering, Chongqing Key Laboratory of Soft-Matter Material Chemistry and Function Manufacturing, Southwest University, Chongqing 400715, China*

Le Yang − *School of Chemical Engineering and Technology, Guangdong Engineering Technology Research Center for Platform Chemicals from Marine Biomass and Their Functionalization, Sun Yat-Sen University, Zhuhai 519082, China;* orcid.org/0000-0003-3055-4904

Zhuwan Li − *Hubei Jiaotou Intelligent Testing CO., LTD, Wuhan 430051, China*

Complete contact information is available at: https://pubs.acs.org/10.1021/acssuschemeng.5c01497

Author Contributions

⊥H.G. and H.Z. contributed equally to this paper.

Notes

The authors declare no competing financial interest.

ACKNOWLEDGMENTS

This work was supported by the National Natural Science Foundation of China (22109129) and the Project of Science and Technology Research Program of Chongqing Education Commission of China (KJQN202400210).

REFERENCES

(1) Feng, Y.; Yang, C.; Fang, W.; Huang, B.; Shao, Q.; Huang, X. Anti-poisoned oxygen reduction by the interface modulated Pd@NiO core@shell. *Nano Energy* **2019**, *58*, 234−243.

(2) Valdés-López, V. F.; Mason, T.; Shearing, P. R.; Brett, D. J. L. Carbon monoxide poisoning and mitigation strategies for polymer electrolyte membrane fuel cells − A review. *Prog. Energy Combust. Sci.* **2020**, *79*, No. 100842.

(3) Jin, C.; Liao, Y.; Zhang, A.; Zhao, S.; Wang, R.; Li, J.; Tang, H. Low-Pt anodes with gradient molybdenum isomorphism for high performance and anti-CO poisoning PEMFCs. *Nano Energy* **2024**, *122*, No. 109305.

(4) Xiao, Z.; Zhang, L.; Tan, X.; Sun, K.; Li, J.; Pan, L.; Zou, J.; Li, G.; Wang, D. Advances in Oxygen Defect-Mediated Photothermal Catalytic CO_2 Hydrogenation Reduction. *Adv. Funct. Mater.* **2025**, No. 2500339.

(5) Zhang, C.; Li, P.; Xiao, Z.; Zhang, H.; Yuan, E.; Gu, J.; Wang, J.; Li, G.; Wang, D. Tuning the CO_2 Hydrogenation Activity and Selectivity by Highly Dispersed Ni−In Intermetallic Alloy Compounds. *ACS Sustainable Chem. Eng.* **2024**, *12* (1), 166−177.

(6) Ray, K.; Deo, G. A potential descriptor for the CO_2 hydrogenation to CH_4 over Al_2O_3 supported Ni and Ni-based alloy catalysts. *Appl. Catal., B* **2017**, *218*, 525−537.

(7) Fu, H.; Sun, S.; Lian, H. Enhanced low-temperature CO_2 methanation over Ni/ ZrO_2-Al_2O_3 catalyst: Effect of Al addition on catalytic performance and reaction mechanism. *J. CO2 Util.* **2023**, *69*, No. 102415.

(8) Wu, X.; Li, L.; Song, M.; Cai, H.; Yang, J.; Li, G.; Hu, C. Insight into the impacts of MnO_2 crystal phases on CO_2 selective hydrogenation to CH_4 on Ni/MnO_x catalysts. *J. CO2 Util.* **2023**, *75*, No. 102584.

(9) Bao, S.; Liu, T.; Fu, H.; Xu, Z.; Qu, X.; Zheng, S.; Zhu, D. $Ni_{12}P_5$ Confined in Mesoporous SiO_2 with Near-Unity CO Selectivity and Enhanced Catalytic Activity for CO_2 Hydrogenation. *ACS Appl. Mater. Interfaces* **2023**, *15* (39), 45949−45959.

(10) Shen, L.; Zhang, W.; Feng, Y.; Xu, J.; Zhu, M. Revealing the promoting effect of Zn on Ni-based CO_2 hydrogenation catalysts. *J. Mater. Chem. A* **2023**, *11* (15), 8248−8255.

(11) Park, H.; Park, K.; Jung, K.-D.; Yoon, S. CO_2 hydrogenation into formate and methyl formate using Ru molecular catalysts supported on NNN pincer porous organic polymers. *Inorg. Chem. Front.* **2021**, *8* (7), 1727−1735.

(12) Gaudillere, C.; Navarrete, L.; Serra, J. M. CO_2 hydrogenation on Ru/Ce based catalysts dispersed on highly ordered microchannelled 3YSZ monoliths fabricated by freeze-casting. *Int. J. Hydrogen Energy* **2017**, *42* (2), 895−905.

(13) Deng, B.; Song, H.; Wang, Q.; Hong, J.; Song, S.; Zhang, Y.; Peng, K.; Zhang, H.; Kako, T.; Ye, J. Highly efficient and stable photothermal catalytic CO_2 hydrogenation to methanol over Ru/In_2O_3 under atmospheric pressure. *Appl. Catal., B* **2023**, *327*, No. 122471.

(14) Wang, Q.; Gao, Y.; Tumurbaatar, C.; Bold, T.; Wei, F.; Dai, Y.; Yang, Y. Tuned selectivity and enhanced activity of CO_2 methanation over Ru catalysts by modified metal-carbonate interfaces. *J. Energy Chem.* **2022**, *64*, 38−46.

(15) Dongapure, P.; Bagchi, S.; Mayadevi, S.; Devi, R. N. Variations in activity of Ru/TiO_2 and Ru/Al_2O_3 catalysts for CO_2 hydrogenation: An investigation by in-situ infrared spectroscopy studies. *Mol. Catal.* **2020**, *482*, No. 110700.

(16) Han, L.; Mao, D.; Yu, J.; Guo, Q.; Lu, G. C_2-oxygenates synthesis through CO hydrogenation on SiO_2-ZrO_2 supported Rh-based catalyst: The effect of support. *Appl. Catal., A* **2013**, *454*, 81−87.

(17) Cao, F.; Gong, N.; Ma, Z.; Wang, X.; Tan, M.; Wu, Y.; Tan, Y. Controlling CO_2 hydrogenation selectivity by Rh-based catalysts with different crystalline phases of TiO_2. *Chem. Commun.* **2022**, *58* (26), 4219−4222.

(18) Cao, F.; Gong, N.; Ma, Z.; Wang, X.; Tan, M.; Wu, Y.; Tan, Y. Correction: Controlling CO_2 hydrogenation selectivity by Rh-based catalysts with different crystalline phases of TiO_2. *Chem. Commun.* **2023**, *59* (16), 2327.

(19) Chen, W.; Ding, Y.; Xue, F.; Song, X.; Ning, L. Highly efficient β-SiC-supported 0.5% Rh-based catalyst for CO hydrogenation to C_2 oxygenates. *Catal. Commun.* **2016**, *85*, 44−47.

(20) Heyl, D.; Rodemerck, U.; Bentrup, U. Mechanistic Study of Low-Temperature CO_2 Hydrogenation over Modified Rh/Al_2O_3 Catalysts. *ACS Catal.* **2016**, *6* (9), 6275−6284.
(21) Srivastava, V. Active Heterogeneous Ru Nanocatalysts for CO_2 Hydrogenation Reaction. *Catal. Lett.* **2016**, *146* (12), 2630−2640.
(22) Wang, C.; Sun, H.; Liu, X.; Jin, X.; Feng, Y.; Shi, H.; Wang, D.; Zhang, Y.; Wang, Y.; Yan, Z. Low-temperature CO_2 methanation over Ru/CeO_2: Investigation into Ru loadings. *Fuel* **2023**, *345*, No. 128238.
(23) Rontogianni, A.; Chalmpes, N.; Nikolaraki, E.; Botzolaki, G.; Androulakis, A.; Stratakis, A.; Zygouri, P.; Moschovas, D.; Avgeropoulos, A.; Karakassides, M. A.; Gournis, D. P.; Tsatsos, S.; Kyriakou, G.; Boukos, N. K.; Panagiotopoulou, P.; Yentekakis, I. V. Efficient CO_2 hydrogenation over mono- and bi-metallic RuNi/MCM-41 catalysts: Controlling CH_4 and CO products distribution through the preparation method and/or partial replacement of Ni by Ru. *Chem. Eng. J.* **2023**, *474*, No. 145644.
(24) Panagiotopoulou, P.; Kondarides, D. I.; Verykios, X. E. Selective methanation of CO over supported Ru catalysts. *Appl. Catal., B* **2009**, *88* (3−4), 470−478.
(25) Truszkiewicz, E.; Bielecka, A.; Moszyński, D.; Ostrowski, A. Lowering risk of methanation of carbon support in Ru/carbon catalysts for CO methanation by adding lanthanum. *Int. J. Hydrogen Energy* **2023**, *48* (64), 24936−24950.
(26) Qiao, B.; Wang, A.; Yang, X.; Allard, L. F.; Jiang, Z.; Cui, Y.; Liu, J.; Li, J.; Zhang, T. Single-atom catalysis of CO oxidation using Pt1/FeOx. *Nat. Chem.* **2011**, *3* (8), 634−641.
(27) Gao, C.; Low, J.; Long, R.; Kong, T.; Zhu, J.; Xiong, Y. Heterogeneous Single-Atom Photocatalysts: Fundamentals and Applications. *Chem. Rev.* **2020**, *120* (21), 12175−12216.
(28) Han, L.; Cheng, H.; Liu, W.; Li, H.; Ou, P.; Lin, R.; Wang, H.-T.; Pao, C.-W.; Head, A. R.; Wang, C.-H.; Tong, X.; Sun, C.-J.; Pong, W.-F.; Luo, J.; Zheng, J.-C.; Xin, H. L. A single-atom library for guided monometallic and concentration-complex multimetallic designs. *Nat. Mater.* **2022**, *21* (6), 681−688.
(29) Singh, B.; Gawande, M. B.; Kute, A. D.; Varma, R. S.; Fornasiero, P.; McNeice, P.; Jagadeesh, R. V.; Beller, M.; Zbořil, R. Single-Atom (Iron-Based) Catalysts: Synthesis and Applications. *Chem. Rev.* **2021**, *121* (21), 13620−13697.
(30) Lang, R.; Du, X.; Huang, Y.; Jiang, X.; Zhang, Q.; Guo, Y.; Liu, K.; Qiao, B.; Wang, A.; Zhang, T. Single-Atom Catalysts Based on the Metal−Oxide Interaction. *Chem. Rev.* **2020**, *120* (21), 11986−12043.
(31) Xia, P.; Wang, C.; He, Q.; Ye, Z.; Sirés, I. MOF-derived single-atom catalysts: The next frontier in advanced oxidation for water treatment. *Chem. Eng. J.* **2023**, *452*, No. 139446.
(32) Yun, R.; Xu, R.; Shi, C.; Zhang, B.; Li, T.; He, L.; Sheng, T.; Chen, Z. Post-modification of MOF to fabricate single-atom dispersed hollow nanocages catalysts for enhancing CO_2 conversion. *Nano Res.* **2023**, *16* (7), 8970−8976.
(33) Jiang, R.; Li, L.; Sheng, T.; Hu, G.; Chen, Y.; Wang, L. Edge-Site Engineering of Atomically Dispersed $Fe−N_4$ by Selective C−N Bond Cleavage for Enhanced Oxygen Reduction Reaction Activities. *J. Am. Chem. Soc.* **2018**, *140* (37), 11594−11598.
(34) Yang, J.; Zeng, D.; Zhang, Q.; Cui, R.; Hassan, M.; Dong, L.; Li, J.; He, Y. Single Mn atom anchored on N-doped porous carbon as highly efficient Fenton-like catalyst for the degradation of organic contaminants. *Appl. Catal., B* **2020**, *279*, No. 119363.
(35) Yang, Y.; Zhao, C.; Qiao, X.; Guan, Q.; Li, W. Regulating the coordination environment of Ru single-atom catalysts and unravelling the reaction path of acetylene hydrochlorination. *Green Energy Environ.* **2023**, *8* (4), 1141−1153.
(36) Li, Z.; Liu, F.; Chen, C.; Jiang, Y.; Ni, P.; Song, N.; Hu, Y.; Xi, S.; Liang, M.; Lu, Y. Regulating the N Coordination Environment of Co Single-Atom Nanozymes for Highly Efficient Oxidase Mimics. *Nano Lett.* **2023**, *23* (4), 1505−1513.
(37) Wang, X.; Chen, Z.; Zhao, X.; Yao, T.; Chen, W.; You, R.; Zhao, C.; Wu, G.; Wang, J.; Huang, W.; Yang, J.; Hong, X.; Wei, S.; Wu, Y.; Li, Y. Regulation of Coordination Number over Single Co Sites: Triggering the Efficient Electroreduction of CO_2. *Angew. Chem., Int. Ed.* **2018**, *57* (7), 1944−1948.
(38) Qiao, B.; Liu, J.; Wang, Y.-G.; Lin, Q.; Liu, X.; Wang, A.; Li, J.; Zhang, T.; Liu, J. J. Highly Efficient Catalysis of Preferential Oxidation of CO in H_2-Rich Stream by Gold Single-Atom Catalysts. *ACS Catal.* **2015**, *5* (11), 6249−6254.
(39) Lou, Z.; Li, W.; Yuan, H.; Hou, Y.; Yang, H.; Wang, H. Structural rule of N-coordinated single-atom catalysts for electrochemical CO_2 reduction. *J. Mater. Chem. A* **2022**, *10* (7), 3585−3594.
(40) Dou, M.; Zhang, M.; Chen, Y.; Yu, Y. DFT study of In_2O_3-catalyzed methanol synthesis from CO_2 and CO hydrogenation on the defective site. *New J. Chem.* **2018**, *42* (5), 3293−3300.
(41) Rocabado, D. S. R.; Aizawa, M.; Ishimoto, T. Predicting CO Interaction and Activation on Inhomogeneous Ru Nanoparticles Using Density Functional Theory Calculations and Machine Learning Models. *J. Phys. Chem. C* **2023**, *127* (47), 23010−23022.
(42) Zhao, W.; Xu, G.; He, Z.; Cai, C.; Abild-Pedersen, F.; Wang, T. Toward Carbon Monoxide Methanation at Mild Conditions on Dual-Site Catalysts. *J. Am. Chem. Soc.* **2023**, *145* (15), 8726−8733.
(43) Zhang, S.-T.; Yan, H.; Wei, M.; Evans, D. G.; Duan, X. Hydrogenation mechanism of carbon dioxide and carbon monoxide on Ru(0001) surface: a density functional theory study. *RSC Adv.* **2014**, *4* (57), 30241−30249.
(44) Song, C.; Liu, J.; Wang, R.; Tang, X.; Wang, K.; Gao, Z.; Peng, M.; Li, H.; Yao, S.; Yang, F.; Lu, H.; Liao, Z.; Wen, X.-D.; Ma, D.; Li, X.; Lin, L. Engineering MOx/Ni inverse catalysts for low-temperature CO_2 activation with high methane yields. *Nat. Chem. Eng.* **2024**, *1* (10), 638−649.
(45) Zhou, Y.; Zheng, P.; Gao, J.; Xu, W.; Yang, Y.; Zhang, L.; Zhu, T.; Xu, G.; Zhong, Z.; Su, F. Suppressing Metal-Support Interaction Enhances Photothermal CO_2 Methanation on the Ru/CeO_2 Catalysts. *ACS Catal.* **2024**, *14* (19), 14285−14296.
(46) Ai, H.; Yang, H.; Liu, Q.; Zhao, G.; Yang, J.; Gu, F. ZrO2-modified $Ni/LaAl_{11}O_{18}$ catalyst for CO methanation: Effects of catalyst structure on catalytic performance. *Chin. J. Catal.* **2018**, *39* (2), 297−308.
(47) Shi, Z.; Feng, J.; Dong, X. Ru−Ni/GA-MMO composites as highly active catalysts for CO selective methanation in H_2-rich gases. *Int. J. Hydrogen Energy* **2023**, *48* (64), 24640−24651.
(48) Lee, Y.-J.; Kang, K.; Kim, C.; Kirk, J.; Sohn, H.; Choi, S. H.; Nam, S. W.; Kim, J.; Jeong, H.; Kim, Y. Pore surface engineering of Al_2O_3-supported Ru catalysts with TiO_2 for enhanced selective CO methanation. *Appl. Surf. Sci.* **2024**, *657*, No. 159551.

https://doi.org/10.1021/acssuschemeng.5c01497
ACS Sustainable Chem. Eng. XXXX, XXX, XXX−XXX